

Accepted Manuscript

Quasi-Static Impact of Indented Foldcores

J.M. Gattas, Z. You

PII: S0734-743X(14)00125-0

DOI: [10.1016/j.ijimpeng.2014.06.001](https://doi.org/10.1016/j.ijimpeng.2014.06.001)

Reference: IE 2353

To appear in: *International Journal of Impact Engineering*

Received Date: 22 October 2013

Revised Date: 9 May 2014

Accepted Date: 1 June 2014

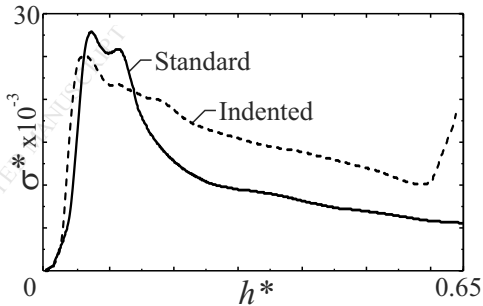
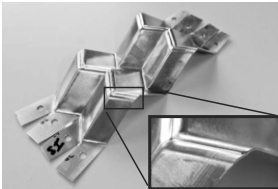
Please cite this article as: Gattas JM, You Z, Quasi-Static Impact of Indented Foldcores, *International Journal of Impact Engineering* (2014), doi: 10.1016/j.ijimpeng.2014.06.001.

This is a PDF file of an unedited manuscript that has been accepted for publication. As a service to our customers we are providing this early version of the manuscript. The manuscript will undergo copyediting, typesetting, and review of the resulting proof before it is published in its final form. Please note that during the production process errors may be discovered which could affect the content, and all legal disclaimers that apply to the journal pertain.



graphical_abstract.pdf

Foldcore

Indented
Foldcore

Highlights: Quasi-Static Impact of Indented Foldcores

- Sub-folds are introduced into a standard foldcore to make an indented foldcore.
- The indented foldcore possessed a high-order travelling hinge line (THL) failure mode.
- The THL failure mode can absorb more energy in a more uniform manner than a standard failure mode.
- Improvements in energy absorption by up to 39% were seen, with a 35% improved uniformity.
- Good correlation is seen between numerical and experimental results.

Quasi-Static Impact of Indented Foldcores

J.M.Gattas^a, Z.You^{b,*}

^a*School of Civil Engineering, University of Queensland, St Lucia, QLD 4072, Australia*

^b*Department of Engineering Science, University of Oxford, Parks Road, Oxford, OX1 3PJ, U.K.*

Abstract

A modified planar foldcore geometry was developed by introducing sub-folds into a standard foldcore pattern. It was demonstrated using numerical simulation that the new geometry, deemed the indented foldcore, successfully triggered a high-order travelling hinge line failure mode. This was found to have a much higher and more uniform energy absorption than the plate buckling failure mode seen in a standard foldcore structure. A numerical analysis also established optimum standard and indented geometries with maximum energy absorption. Prototypes were constructed to experimentally validate numerical findings. Prototypes with no visible geometric imperfections displayed the travelling hinge line behaviour as predicted. Prototypes with visibly-buckled plates showed no change in failure mode compared to a standard foldcore, confirming numerical findings that the travelling hinge line failure mode is highly sensitive to geometric imperfections.

Keywords: rigid origami, foldcore, indented foldcore, quasi-static impact

*Corresponding author

Email address: zhong.you@eng.ox.ac.uk (Z.You)

1. Introduction

1.1. Sandwich Panels

The energy absorption capabilities of sandwich panel elements are extensively studied in literature. For high-performance applications with demanding weight-specific stiffness and energy absorption capabilities, hexagonal honeycomb cores are commonly employed. When loaded in an out-of-plane direction, the hexagonal core geometry generates an extremely high initial peak force, followed by an oscillating post-failure reaction force as sequential folding elements form in the core cell walls [1, 2]. This failure mode forms a large number of static hinge lines across the honeycomb core, resulting in a high average reactive force and a large amount of energy absorption [3, 4, 5]. Despite this high average force, the failure mode is very non-uniform, in that there is a large difference between peak and average reaction forces. Various methods to improve the honeycomb uniformity have been suggested, including pre-crushing the honeycomb core [6], however this effect can be negated at dynamic loading [7].

Eggbox cores are another core structure that can be designed to have a very efficient energy absorbing failure mode. At certain configurations, the eggbox core possesses a *travelling hinge line* failure mode, in which shell inversion occurs at the narrow end of the conical eggbox unit and propagates through the core along a circular travelling hinge line [8]. This plasticizes a large area of core material twice, once as it rolled into the travelling hinge line and again when it unrolled out of the travelling hinge line, and as such absorbs large amounts of energy. The eggbox core exhibits a low reaction force at the initial inversion, and then the reaction force gradually increases as the travelling hinge line expands across a larger cross-section of the conical

unit, Figure 1(a). The failure mode is very sensitive to imperfections, which cause the core to revert to a non-symmetric failure mode [8]. This sensitivity is a problematic attribute for an energy absorbing device and so the eggbox core is rarely employed.

Foldcore sandwich panels have been suggested as a potential substitute, as they possess a number of favourable properties that are not possible with other types of high-performance sandwich panel [9], e.g. isotropic strength coefficients [10] and continuous manufacture [11]. Under out-of-plane impact, they exhibit a plate buckling failure mode [9, 12], typified by a high initial force followed by a steep post-buckling reduction in force. The high initial force occurs from the high buckling resistance of the parallelogram core plates, which are all continuously supported on four sides. The post-buckling force reduction occurs as collapse is about stationary hinge lines formed across buckled plate regions. The foldcore therefore possesses the same drawback as the honeycomb core, namely a non-uniform force-displacement response.

1.2. Indented Foldcore

A previous study by Ma and You [13] has used rigid-origami design principles to pre-fold the surface of a tube based on an origami pattern. The pre-folded tube has a failure mode that differs from the standard thin-walled tube failure modes. The new failure mode, known as the complete diamond mode, led to a higher amount of energy absorption and good load uniformity. This paper subjects the standard foldcore to a similar procedure to generate a modified foldcore geometry with improved energy absorption capabilities under out-of-plane impact loading. Deemed the *indented foldcore*, it is created by placing sub-folds in a standard foldcore, which act as a line

imperfection that triggers an initial plate failure at the core ridge, and the subsequent formation of top-down travelling hinge line. This failure mode is similar to the failure mode of the eggbox core, with the difference being that the hypothesised travelling hinge line maintains an almost constant length throughout the duration of the crush, Figure 1(b), to create a high, near-uniform force-displacement response.

The behaviour of an indented foldcore, and its performance relative to a standard foldcore, is assessed as follows. Section 2 establishes a geometric parametrisation of a standard and indented foldcore. Section 3 conducts a numerical parametric study on foldcore periodic unit geometries, to establish an optimum standard and indented configuration. An experimental analysis is given in Section 4 and Section 5 presents a discussion and comparison between numerical and experimental results.

2. Standard and Indented Foldcore Parametrisation

A standard foldcore corresponds to a rigid origami pattern known as a Miura pattern. There are numerous ways to parametrise this pattern, however this paper adopts the parametrisation given in [14], in which a standard unit cell is defined with four parameters: side lengths a and b , pattern angle ϕ , and a single pattern variable to define the folded configuration, for example longitudinal or lateral edge angle η_A or η_Z , Figure 2(a). These latter two parameters are related by:

$$(1 + \cos \eta_Z)(1 - \cos \eta_A) = 4 \cos^2 \phi \quad (1)$$

An additional plate thickness parameter t_p is needed as the foldcore sheet has non-zero thickness. This is used to calculate core density $\alpha = V_p/V$, which

is the volume of core plates $V_p = 4abt_p \sin \phi$ contained in a unit volume $V = l_a l_b l_t$, where length $l_a = 2a \sin(\eta_A/2)$, width $l_b = 2b \sin(\eta_Z/2)$, and height $l_t = a \cos(\eta_A/2)$.

The indented foldcore geometry is simply created by introducing a small indent along top ridge of standard foldcore pattern, Figure 2(b). It can be seen from the indented foldcore crease pattern that the indent can be thought of as a short, inverted Miura pattern with side length a_i , where the subscript i denotes indent. For geometric compatibility, the inverted Miura segment must have the same b , ϕ , and η_Z as the main plate segment. Therefore a single extra dimensional constant, a_i , is sufficient to uniquely define an indented pattern. It is convenient to define the standard side length $a_s = a - a_i$, the dimensionless indented ratio $p^* = a_i/a$, and the dimensionless side length aspect $b^* = b/a$. Henceforth the superscript $*$ shall be used to denote dimensionless parameters. An indented foldcore with the same a , b^* , ϕ , and η_A parameters as a given standard foldcore will have identical l_a and l_b values, but a reduced height of $l_t = a_s \cos(\eta_A/2)$.

3. Numerical Analysis

3.1. Parametric Model Geometry

A numerical study was conducted on indented foldcore parameters to assess if and when it exhibited the desired failure mode. There are five parameters of interest: ϕ , η_A , and η_Z , which control the configuration of the core plates, and b^* and p^* , which control the aspect ratios of the core plates. The effect of density parameter α is considered separately in Section 3.5 and the sensitivity of cores to geometric imperfections considered in Section 3.6. To efficiently explore this large configuration space, parametric models were

generated by independently altering a single parameter of a base geometry. This base geometry was deemed A1 and was set as $a = 30\text{mm}$, $b^* = 0.5$, $p^* = 1/15$, $\alpha = 4\%$, $\phi = 60^\circ$, $\eta_Z = 109.5^\circ$, and $\eta_A = 120.0^\circ$.

Four models were generated for each of the three configuration parameters, with geometry chosen to create good distribution across the configuration space of Equation (1), see Figure 3 and Table 1(a). B models possess a common ϕ parameter and so represent different folded configurations of the same base pattern. C models possess a constant η_A parameter so represent different lateral steepness configurations. Similarly, D models possess a constant η_Z and correspond to different longitudinal steepness configurations. Four models were also generated for b^* and p^* aspect ratio parameters, see Figure 3(b) and Table 1(b). E models have varied side length aspects where $0.125 \leq b^* \leq 2$. F models have varied indent aspects where $0 \leq p^* \leq 0.25$.

Seventeen equivalent standard models, A1^s-E5^s, were also generated with the same parameter values above, excluding p^* which is set to zero and therefore excludes the four indent aspect F models. Note that the superscript *s* is used henceforth to indicate a standard foldcore.

3.2. Numerical Method

A numerical simulation of all cores being crushed between two rigid bodies was conducted using a quasi-static, large-displacement analysis in finite element software ABAQUS/Explicit. The core mesh was constructed with S4R shell elements with mesh size approximately equal to $a/80$. This mesh density was selected after a mesh convergence study showed values for crush stress converged at approximately this size, with a 2% change from $a/48$ to $a/96$. A small bend radius was used in place of the sharp ridge crease lines seen in the idealised origami geometry, as this is a more realistic approxima-

tion of the shape of a formed metallic foldcore. A proportionally equal bend radius, equal to $a/40$, was used for all models. A ductile, annealed, pure aluminium material was selected for the analysis, with isotropic elastic-plastic material properties of $E = 69\text{GPa}$, $\nu = 0.33$, $\sigma_Y = 28\text{MPa}$, $\sigma_U = 83\text{MPa}$, $\rho = 2710\text{kg/m}^3$, and strain hardening data obtained from material sample tests shown in Table 2(a).

Fixed boundary conditions were applied along the four base edges, and periodic boundary constraints applied along side edges. Loading was applied by crushing the structure between two rigid panels, with the top plate given smooth-step crush displacement of up to approximately $65\%l_t$. To ensure a quasi-static analysis, the loading velocity was set at 2m/s , which limited the kinetic energy to internal energy ratio to be less than 5%, as recommended in the Abaqus User Manual [15]. Comparative numerical models, with slower impact velocities and reduced mass properties, displayed no change in behaviour from the above analysis, confirming it is a quasi-static rate with no dynamic inertial or strain rate sensitivity behaviours. Top panel contact, bottom panel contact, and self-self contact were all modelled with surface-surface tangential friction, with a friction coefficient of 0.25.

Core performance is assessed using criteria from [16], which states that a good energy absorption device should have, amongst other properties, a restricted and uniform reactive force, a long crush displacement, and a high Specific Energy Absorption capacity (SEA). These attributes can be read from a core force-displacement response, measured as the reacting force on the top plate when impacting the core unit. To facilitate comparison between the models, crush force P and crush displacement h are normalised to dimensionless stress and strain parameters $\sigma^* = \sigma/\sigma_Y = P/(l_a l_b \sigma_Y)$ and $h^* = h/l_t$,

respectively. The dimensionless energy absorption E^* is the integral of dimensionless stress-strain curve, and the total energy absorbed, E_d^* , is attained at the densification strain h_d^* . The densification strain was set at the point at which the crush stress began to sharply rise, or 60%, whichever is less. From these values, the average dimensionless stress is calculated as, $\sigma_{avg}^* = E_d^*/h_d^*$. The uniformity ratio U^* is defined as $U^* = \sigma_{max}^*/\sigma_{avg}^* = P_{max}/P_{avg}$, where an ideal energy absorbing device would possess a U^* value approaching unity. An optimum core configuration is defined as the core possessing the highest σ_{avg}^* and lowest U^* .

3.3. Indented Simulation Results and Discussion

Dimensionless stress-strain responses and representative failure modes for the indented pattern configuration models A1-D5 are shown in Figure 4 and relevant values listed in Table 3. A range of failure modes are seen which can generally be classified as one of three types. Type 1 models, B1 and D1, exhibit plate buckling behaviour, typified by a sharp initial peak force followed by a steep drop in reaction force. From the B1 stress plot, Figure 5(a), it can be seen that the initial buckle location remains stationary for the crush duration.

Type 2 models, B3 and C3, show the start of a travelling hinge line (THL) failure mode, typified by a double-peak in the force-displacement plot. From the C3 stress plot, Figure 5(b), it can be seen that this double-peak corresponds to an initial inversion about the indent, a slight dip in strength as this buckle propagates, and then a second peak prior to the onset of plate buckling. Duration of the second peak, which represents the time before the travelling hinge is lost to plate buckling behaviours, varies considerably for each model. In model C1 this secondary buckling occurs almost immediately

after initial inversion at $h^* = 10\%$, and so the failure mode is actually initial and secondary formation of static hinge lines, rather than a travelling hinge line. However in model C3, plate buckling does not occur until approximately $h^* = 35\%$, and so the second static hinge lines propagate to form travelling hinge lines.

Type 3 models, B5, D4, C5, and D5, show initial buckling around the top indent, followed by buckling and rotation about the the base supports, see Figure 5(c). Both the initial buckle and subsequent rotation occur at low stress, so the reaction stress is low but uniform. Note that these three classifications are not discrete, with most cores exhibiting a combination of the three types. Models C1, C2, and B2 show type 1 and 2 modes. Models A1 and D2 show type 2 and 3 modes.

Relevant energy absorption values from Table 3 are plotted in energy absorption suitability charts, that is uniformity versus average reaction stress, in Figure 4. It can be seen that steep type 1 models have reasonably high values of σ_{avg}^* but generally poor U^* , due to the sharp reduction in reaction stress following the initial buckle. Shallow type 3 models give a poor σ_{avg}^* but generally good U^* . Type 2 exist between these two extremes and allow travelling hinge formation and propagation at high stress levels, giving a very high σ_{avg}^* with a low U^* , the desired core attributes. Model C3, with the largest area swept through by the travelling hinge line, has exceptional energy absorption properties. It has the highest σ_{avg}^* and the lowest, near-ideal uniformity of $U^* = 1.2$. This shows that the travelling hinge line corresponds to a smaller disparity between the peak and average stress, and therefore a much better energy absorption capability.

Dimensionless stress-strain responses and representative failure modes for

the b^* aspect ratio configuration models E1-E5 are shown in Figure 6(a) and Table 3. For E models, three distinct failure modes are seen. The narrowest model E5, with $b^* = 0.125$, shows a beam buckling failure mode, typified by an initial peak stress followed by an immediate post-buckling stress reduction. The widest model E1, with $b^* = 2$, has a plate buckling mode that is similar to the beam buckling mode, but with a less severe post-buckling stress reduction. Inspection of the plate stresses of these two models, Figure 6(b), shows that the plate aspect of model E5 is too narrow to cause plate buckling and the plate aspect of model E1 is too wide to allow a travelling hinge line to form. The middle aspect ratio, model E3 with $b^* = 0.5$, exhibits the previously seen type 2 travelling hinge failure mode. In terms of energy absorption suitability, the beam buckling mode is least suited, with a very high U^* , and the travelling hinge line mode is again better suited than the plate buckling mode.

Indented aspect p^* model results are shown in Figure 7. It can be seen that there is no change in the failure model from F1 to F2, indicating that a minimum threshold indent depth must be reached before the indent is effective at changing the core failure mode. In this case the minimum threshold is reached in model F3 with $p^* = 0.05$. Increasing the indent depth significantly beyond this minimum threshold does not provide any further advantage, with models F4 and F5 both having less optimal performance in terms of energy absorption capabilities.

To summarise, the twenty-one indented model results have been collated and plotted in Figure 8(a). It can be seen that model C3 is the optimum indented model, with a 123.1% improvement in σ_{avg}^* and a 7.7 % reduction in U^* , compared to the initial geometry A1. Model C3 had the largest area

swept through by a travelling hinge line, confirming the hypothesis that an indent can force this mode, and that when present, the travelling hinge is an extremely efficient energy absorption mechanism.

3.4. Standard Simulation Results and Discussion

The results of the seventeen standard foldcore models A1^s-E5^s have been collated and plotted in Figure 8(b) and Table 4. The effect of individual parameters is not discussed as most standard models simply exhibited plate-buckling type failures. It can be seen that the standard configuration with the highest σ_{avg}^* is C2^s, with a 152.3% improvement in σ_{avg}^* and a 7.4% increase in U^* compared to the initial model A1^s. Also highlighted in Figure 8(b) is model C3^s, which is seen to have a 22.3% lower σ_{avg}^* compared to model C2^s. Indented and standard foldcores are therefore seen to have different optimum configurations, with C3 optimum for the former and C2^s optimum for the latter.

Two comparisons can be made between standard and indented cores. Comparing C3 and C3^s, it can be seen that the indented model offers a significant improvement, with a large increase of 19.6% in σ_{avg}^* and a large reduction of 45.4% in U^* . Comparing C3 and C2^s, Figure 8(c), the indented model is again seen to be an improvement, with a slight reduction of 7.2% in σ_{avg}^* but a large reduction of 50.7% in U^* . By either comparison, it can be seen that the indented core, at an optimum configuration that allows travelling hinge line formation, is much better suited for energy absorption applications requiring a uniform stress response. Note that for these comparisons, consideration was given to both σ_{avg}^* and U^* , as the twin primary goals of indented foldcore were to improve on the standard foldcore uniformity while maintaining or improving σ_{avg}^* .

Figure 9 shows the hinge formation and stress propagation for the C3 and C2^s models. It can clearly be seen that the uniform indented response is due to a very stable travelling hinge line progression. The initial hinge formation at the top ridge of the pattern keeps the remaining plate area relatively undistorted, allowing the inversion to propagate and the resisting stress to remain high. By comparison, the standard core has a higher initial stress because the initial plate buckle plasticises a larger area. However this distorts the rest of the core plates, and the core subsequently collapses at a reduced stress level. If model C3 is taken as an optimum travelling hinge line failure mode, and model C2^s is taken as an optimum plate buckling failure mode, it can be concluded that the travelling hinge line is better suited for energy absorption purposes.

3.5. Density Parameter Study

Models C3 and C2^s were rerun with different densities of $\alpha = 2\%, 6\%$, and 8% to assess the effect core density has on relative performance. These results, along with the original $\alpha = 4\%$ models, are listed in Table 5 and plotted in Figure 10. It can be seen that the usefulness of indent fades at higher densities, that is to say that in comparison to standard models at the same density, the indented models have an increasingly lower σ_{avg}^* and decreasingly lower U^* , as the density increases. Inspection of two stress-displacement curves at a higher density, Figure 10(b), shows that the travelling hinge line failure mode is still present, however it does not appear to strengthen at the rate that the plate buckling mode does. In terms of uniformity, the indented response is approximately constant whereas the standard core improves as the density increases. These two differences combine to erode the benefits of employing an indented foldcore as the density increases.

3.6. Sensitivity Study

In [8], the travelling hinge line failure mode of an eggbox core was shown to be highly sensitive to geometric imperfections. Models C3 and C2^s, with the original core density of $\alpha = 4\%$, were therefore investigated with included geometric imperfections to see whether they exhibit a similar sensitivity. Geometric imperfections were generated by superimposing an original perfect core geometry with buckling mode nodal displacements. For the indented and standard foldcores, the second and first buckled modes, respectively, were found to cause the lowest σ_{avg}^* . Eight geometrically-imperfect models then were set up for both foldcores, corresponding to maximum buckled displacements δ of 25%, 50%, 75%, 100%, 125%, 150%, 175%, and 200% of t_p . Imperfect models were designated FE' $_{\delta/t_p*100}$.

Responses from the sensitivity study models are shown in Figure 11 and key values summarised in Table 6. Figure 11 (a) shows σ_{max}^* and σ_{avg}^* plotted against δ/t_p for indented imperfect models. Indented cores, it can be seen that there is a gradual decline in σ_{max}^* with increasing δ/t_p and a convergence in σ_{avg}^* after approximately $\delta/t_p = 1.0$. Figure 11(c) shows the dimensionless stress-strain responses of numerical models over this range of imperfection magnitudes. It can be seen that the area of the second hinge line steadily decreases and eventually disappears. The base FE model has the full THL upto approximately $h^* = 35\%$, as discussed previously, whereas FE'₇₅ has no secondary hinge line and so is a typical Type 1 plate buckling mode.

Figure 11 (b) shows σ^* against δ/t_p for standard imperfect models. There is an initial steep decline in σ_{max}^* from FE to FE'₂₅, followed by a gradual decline similar to that seen in the indented models. A similar drop occurs initially for σ_{avg}^* , although this value then converges almost immediately after

$\delta/t_p = 0.25$. Again comparing the dimensionless stress-strain responses of selected numerical modes, Figure 11(d), it can be seen that the Type 1 failure mode, plate buckling, occurs in both FE and FE' models, although the slight secondary hinge that formed in the FE model was lost immediately at FE'₂₅.

To conclude, the indented foldcore travelling hinge line Type 2 failure mode was suppressed in the presence of geometric imperfections, with a plate buckling Type 1 exhibited instead. The standard foldcore exhibited the same Type 1 failure mode in both perfect and imperfect geometry models. The indented foldcore is therefore judged to be more sensitive to geometric imperfections than the standard foldcore.

4. Experimental Analysis

4.1. Geometry and Material

Indented foldcore prototypes were constructed from a pure aluminium sheet material at two sheet thicknesses, $t_p = 0.5\text{mm}$ and 1.0 mm . Foldcore height was set at 40mm and remaining parameters chosen to match the optimum indented foldcore configuration, giving $a = 60\text{mm}$, $b = 30\text{mm}$, $\phi = 64.8^\circ$, $\eta_A = 95^\circ$, and $p^* = 1/15$. To facilitate material draw during manufacture, 2mm fillets were also included at the foldcore ridge locations, giving a final unit height of $l_t = 36\text{mm}$. The total core was constructed using four units, two each in the longitudinal and lateral directions, for a global length L , global width W , and density as shown in Table 7. Note the nomenclature for height l_t is replaced with the equivalent global height H for consistency.

Comparative standard foldcores were also constructed with $t_p = 0.5\text{mm}$ and 1.0 sheet, with identical values for a , b , ϕ , and η_A to that used for

the indented foldcore prototype. 2mm fillets were again added at foldcore ridge locations to give global dimensions as shown in Table 7. Note that the C3^s configuration was used, rather than the optimal C2^s configuration, as it simplified manufacture, as discussed next.

4.2. Manufacturing Method

The standard foldcore was formed in a single punch stamping process with the male and female steel dies mounted on a mechanical punch press. The indented core was formed in a two-stage process: a standard core was first formed, then subjected to a second punch in a set of indented forming dies. This simply punched the indent into the core without altering the a_s length of core plates. Table 7 shows the final formed dimensions of all foldcores to the nearest half millimeter. Standard models with $t_p = 0.5\text{mm}$ and 1.0mm are given the models names Mi05 and Mi10, respectively. Similarly, the indented models are named Ind05 and Ind10. It can be seen that the formed dimensions are close to the designed dimensions. Inspection of the plates shows that the Mi10 and Ind10 models formed without significant visual imperfections, Figure 12(a)-(b), however the Mi05 and Ind05 models have some visible buckling ripples, Figure 12(c)-(d).

Three samples of each foldcore type were annealed at 345°C . Tensile tests were conducted on annealed material samples for both sheet thicknesses. The material properties given in Table 2(a) and used for numerical models were the annealed material properties of the 0.5mm thick aluminium sheet. Although ostensibly the same aluminium alloy, the 1mm thick aluminium sheet was found to be a slightly stronger and less ductile material than the 0.5mm sheet, with $\sigma_Y = 37\text{MPa}$, $\sigma_U = 106\text{MPa}$, and strain hardening data as shown in Table 2(b).

4.3. Experimental Method and Results

For testing, the prototypes were restrained by clamping the front and back edge tabs to a rigid baseplate. These were placed into an INSTRON Universal Testing machine and crushed under quasi-static loads, with a rigid top plate descending at a rate of 2mm/min to a crush depth of approximately $65\%H$. Note that this is slower than the 2m/s loading rate used for FE models, in order to allow observation of the experimental failure modes. The difference in rates is not expected to affect later comparisons, as both are a quasi-static loading rates. Dimensionless stress-strain results obtained from testing are shown in Figure 13 and it can be seen that there is good repeatability for all cores.

5. Discussion

5.1. Comparison of 1mm Foldcore Analyses

A comparison of $t_p = 1.0\text{mm}$ numerical and experimental results is shown in Figure 14(a) and Table 8. The numerical results are obtained from models analysed in the same manner as described in the previous chapter, with two differences: 1mm sheet material properties replace the previously used material properties, and the entire core geometry is constructed, rather than a single periodic unit geometry. This is because there are very few foldcore units used in the prototypes, and so it is likely that free edge effects will be significant.

It can be seen that there is good correlation between numerical and experimental predictions for the standard foldcore, with a maximum difference of 18.9% in σ_{avg}^* of Mi10. There is also good correlation between the numerical and experimental predictions for the indented foldcore. It can also

be seen that there are slight discrepancies in the indented numerical and experimental curves, specifically the double-hump shown in the numerical but not the experimental curve. This might be attributable to plate tearing behaviour, which is observed in experimental models but not accounted for in the numerical material definition, Figure 16(c). It might also be due to imperfect formation of the indent.

Finally, a direct comparison of failure modes, Figure 14(b)-(c), shows good correlation between predicted and observed failure modes.

5.2. Comparison of 0.5mm Foldcore Analyses

A comparison of $t_p = 0.5\text{mm}$ numerical and experimental results is shown in Figure 15(a) and Table 8. As plate buckling was evident in the $t_p = 0.5\text{mm}$ models, Figure 13(c)-(d), FE' models with a maximum imperfection magnitude of $200\% \delta/t_p$ were also created. It can be seen that a Type 1 plate buckling mode is exhibited by both Mi05 and Ind05, and that this failure mode is successfully predicted by FE' models. This agrees with results of the sensitivity study in Section 3.6 and so it is concluded that the travelling hinge line failure mode is sensitive to the presence of geometric imperfections, which can cause the indented foldcore to revert to a standard plate buckling type failure.

A direct comparison of failure modes, Figure 15(b)-(c), shows good correlation between predicted and observed failure modes, however there is a larger discrepancy between predicted and observed σ^* values than was observed for the 1.0mm models. Comparing numerical and experimental predictions for the standard foldcore, there is a maximum difference in values of σ_{max}^* and σ_{avg}^* of 54.0% and 33.3%, respectively. For indented cores, this discrepancy is 54.0% and 34.8%, respectively. The discrepancies are thought to arise from

additional imperfect conditions present in the experiment but not in numerical models, for example sample springback following manufacture, and the non-simultaneous impact of the four core unit ridges. However additional modelling was not undertaken to confirm this, as the primary purpose of the present study was to investigate demonstrated failure modes, a purpose for which the present FE' numerical models were adequate.

5.3. Standard and Indented Experimental Comparison

A comparison of averaged experimental results for Mi10 and Ind10 is shown in Figure 16(a). It can be seen that the indent is successful in triggering an improved energy absorbing response, with a reduction in σ_{max}^* of 9.6% and an increase in σ_{avg}^* of 38.6%, compared with the standard model. Inspection of the final crushed cores, Figure 16(b)-(c), shows that their final failure modes are significantly different, with mid-plate buckling in the standard core and ridge buckling indicative of a partial travelling hinge line in the indented core.

A comparison of Mi05 and Ind05 experimental responses is shown in Figure 16(d). It can be seen that the indent does not significantly alter the failure mode of the foldcore, with both standard and indented exhibiting a typical plate buckling failure. Inspection of the final crushed cores, Figure 16(e)-(f), confirms that there is no significant change in the final crushed shape, with mid-plate buckling occurring in both. There is a slight increase in σ_{avg}^* of 7.8% however this is attributable to the increased density of the indented foldcore, rather than a change in failure mode.

6. Conclusion

This paper has demonstrated the energy absorption capabilities of a new, indented foldcore geometry under out-of-plate quasi-static impact loads. A numerical parametric study established an optimum indented geometry. This was seen to possess a travelling hinge line failure mode with a high, uniform reaction stress. In contrast, an optimum standard foldcore was seen to possess a stationary hinge failure mode, which had non-uniform stress response typified by a significant weakening after initial hinge formation. Experimental testing and a numerical sensitivity investigation demonstrated that foldcores constructed with no visible geometric imperfections, that is Mi10 and Ind10, exhibited failure modes and responses as numerically predicted. In foldcores with visible geometric imperfections, that is Mi05 and Ind05, the imperfections were seen to suppress the travelling hinge line failure mode, and thus eliminate the advantage of indented foldcores over standard foldcores.

There were three significant limitations to the work presented here. First, the parametric study was limited, with only five models built for each parameter. Therefore it is possible that a more thorough parametric analysis, particularly in the local configuration space about model C3, would be able to produce a further improved indented geometry. Other sub-fold configurations might also generate a further improved geometry. Second, the cores studied in this paper have all been analysed without attached sandwich panel faces. Intuitively it can be seen that the indented failure mode is not possible in a sandwich panel assembly, a limitation which is likely to limit applications of the indented foldcore. Similarly, other core attributes required for successful sandwich panel application, such as stiffnesses and behaviour under dynamic loads, have not yet been considered. Third, the limited experiments could

not confirm the precise magnitude of geometric imperfections necessary to suppress a travelling hinge line failure mode, but they were sufficient to confirm that this sensitivity exists. Further experimental investigations have not been conducted at this stage, both because of limitations to the current manufacturing method and because the sensitivity of the indented foldcores, similar to that described in the literature review for eggbox cores, is likely to limit energy absorption applications for which it is suitable.

7. Acknowledgements

The authors are grateful for the financial support provided by Air Force Office of Scientific Research R&D Project 134028. The first author is also grateful for the financial support provided by the John Monash Award.

References

- [1] T. Wierzbicki, Crushing analysis of metal honeycombs, *International Journal of Impact Engineering* 1 (1983) 157 – 174. doi:10.1016/0734-743X(83)90004-0.
- [2] T. Wierzbicki, W. Abramowicz, On the crushing mechanics of thin-walled structures, *Journal of Applied Mechanics* 50 (1983) 727–734. doi:10.1115/1.3167137.
- [3] M. Zarei Mahmoudabadi, M. Sadighi, A theoretical and experimental study on metal hexagonal honeycomb crushing under quasi-static and low velocity impact loading, *Materials Science and Engineering: A* 528 (2011) 4958–4966. doi:10.1243/09544062JMES2382.

- [4] M. Giglio, A. Manes, A. Gilioli, Investigations on sandwich core properties through an experimental–numerical approach, *Composites Part B: Engineering* 43 (2012) 361–374. doi:10.1016/j.compositesb.2011.08.016.
- [5] J. Kee Paik, A. K. Thayamballi, G. Sung Kim, The strength characteristics of aluminum honeycomb sandwich panels, *Thin-walled structures* 35 (1999) 205–231. doi:10.1016/S0263-8231(99)00026-9.
- [6] H. Corporation, Hexweb®honeycomb energy absorption systems design data, 2006. URL: <http://www.hexcel.com/Resources/DataSheets/Brochure-Data-Sheets>.
- [7] M. A. Hazizan, W. Cantwell, The low velocity impact response of an aluminium honeycomb sandwich structure, *Composites Part B: Engineering* 34 (2003) 679–687. doi:10.1016/S1359-8368(03)00089-1.
- [8] V. Deshpande, N. Fleck, Energy absorption of an egg-box material, *Journal of the Mechanics and Physics of Solids* 51 (2003) 187–208. doi:10.1016/S0022-5096(02)00052-2.
- [9] S. Heimbs, Foldcore sandwich structures and their impact behaviour: an overview, in: *Dynamic Failure of Composite and Sandwich Structures SE - 11*, volume 192 of *Solid Mechanics and Its Applications*, Springer Netherlands, 2013, pp. 491–544.
- [10] K. Miura, Zeta-core sandwich- its concept and realization, ISAS Report 480, Institute of Space and Aeronautical Science, University of Tokyo (1972) 137–164.

- [11] D. H. Kling, Folding methods, structures and apparatuses, 2006. US Patent App. 11/440,263.
- [12] M. Q. Nguyen, S. S. Jacombs, R. S. Thomson, D. Hachenberg, M. L. Scott, Simulation of impact on sandwich structures, *Composite Structures* 67 (2005) 217–227. doi:DOI:10.1016/j.compstruct.2004.09.018.
- [13] J. Ma, Z. You, Energy absorption of thin-walled square tubes with a pre-folded origami pattern part i: Geometry and numerical simulation, *Journal of Applied Mechanics* 81 (2014) 011003. doi:10.1115/1.4024405.
- [14] J. Gattas, W. Wu, Z. You, Miura-base rigid origami: Parametrisations of first-level derivative and piecewise geometries, *Journal of Mechanical Design* 135 (2013) 111011. doi:10.1115/1.4025380.
- [15] Simulia, ABAQUS 6.9 Analysis User Manual, Simulia Corp., Providence, RI, USA., 2009.
- [16] G. Lu, T. Yu, Energy Absorption of Structures and Materials, Woodhead Publishing Limited, Cambridge, England, 2003.

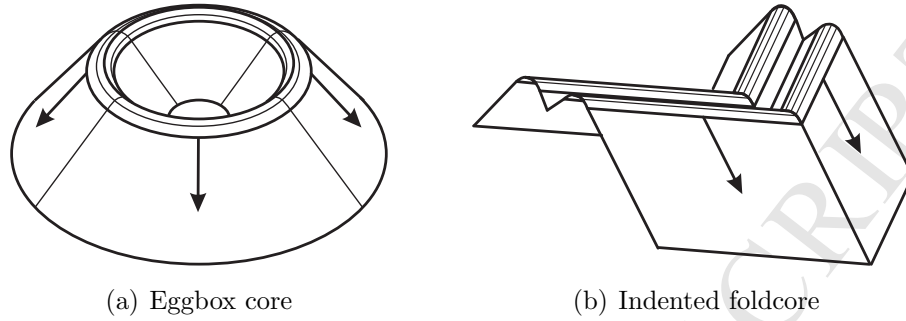


Figure 1: Expanding travelling hinge line failure mode in eggbox core and hypothesised constant length travelling hinge line in indented foldcore.

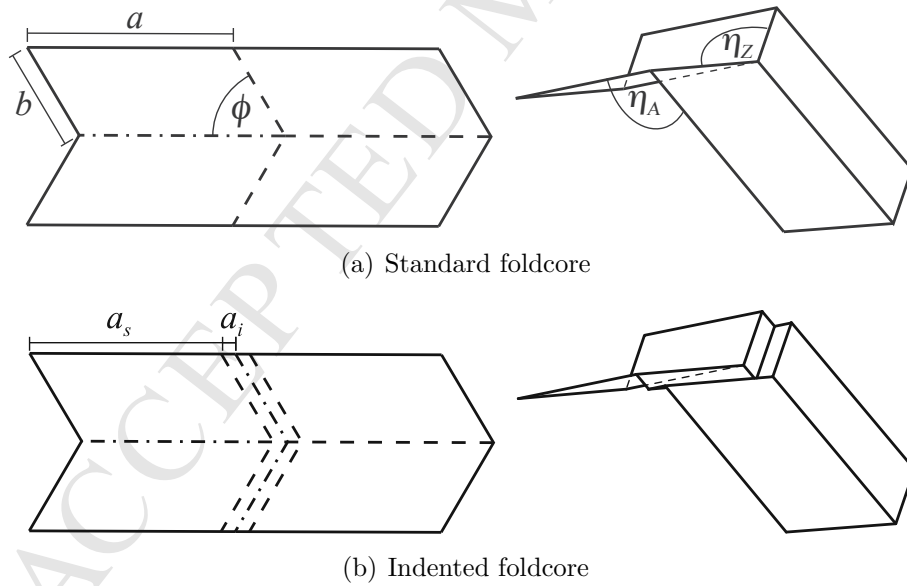


Figure 2: Unfolded crease pattern, on left; folded configuration, on right.

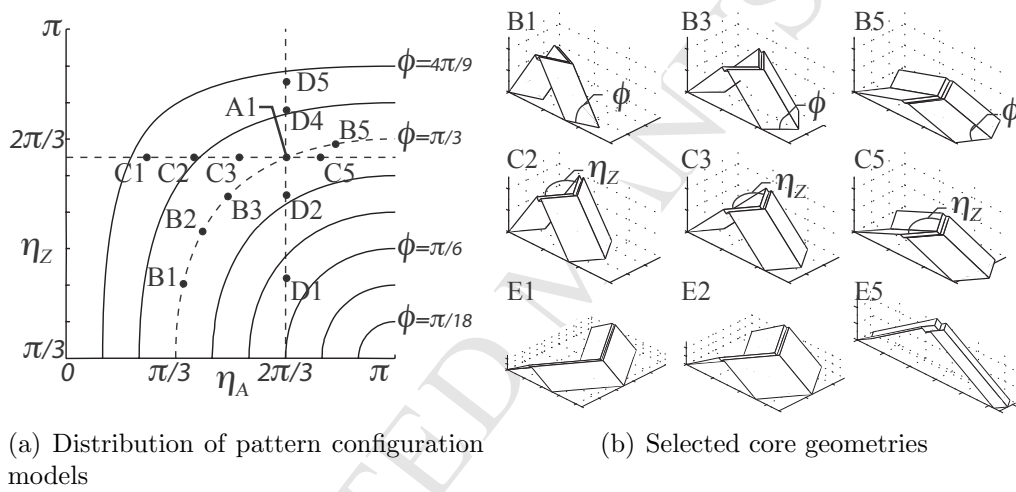
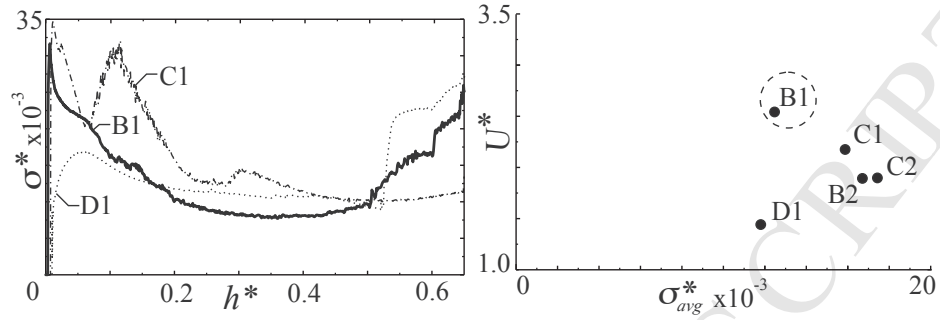
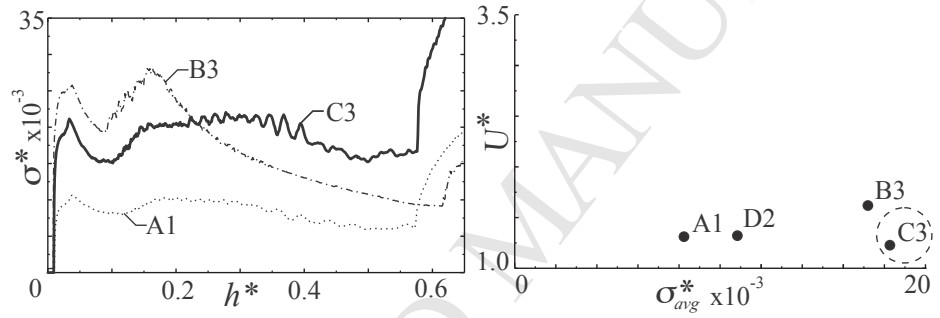


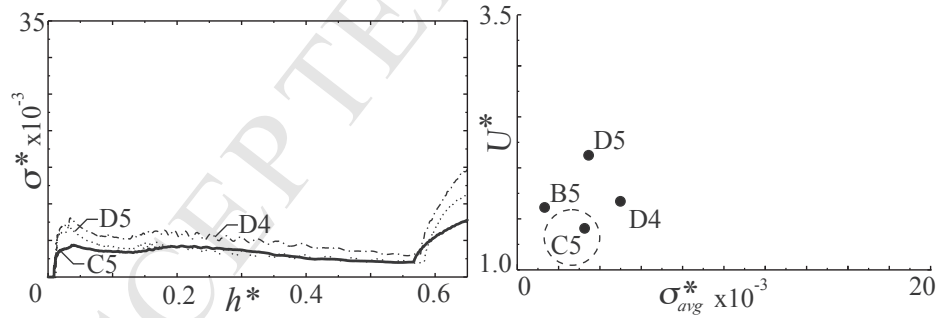
Figure 3: Indented foldcore numerical unit geometries.



(a) Type 1 failure mode



(b) Type 2 failure mode



(c) Type 3 failure mode

Figure 4: Dimensionless stress-strain responses of selected parametric study models, on left; energy absorption suitability, on right.

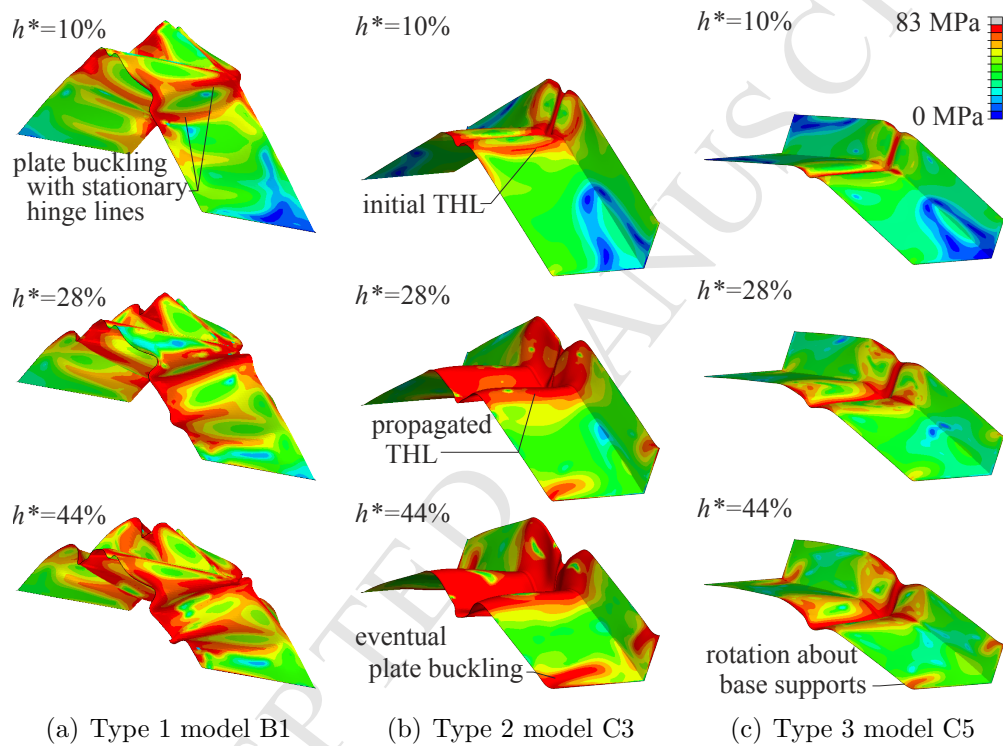
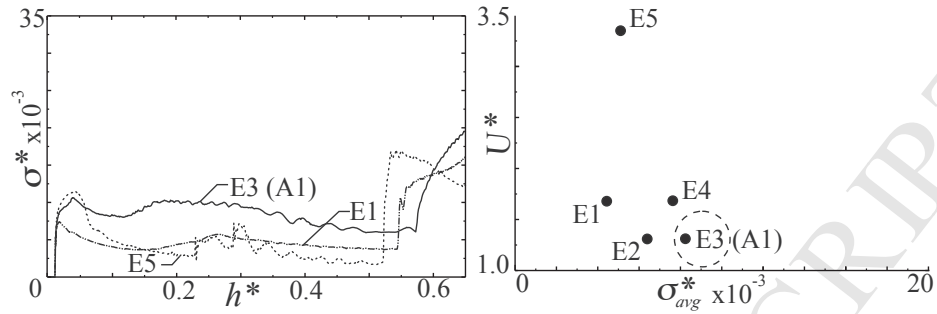
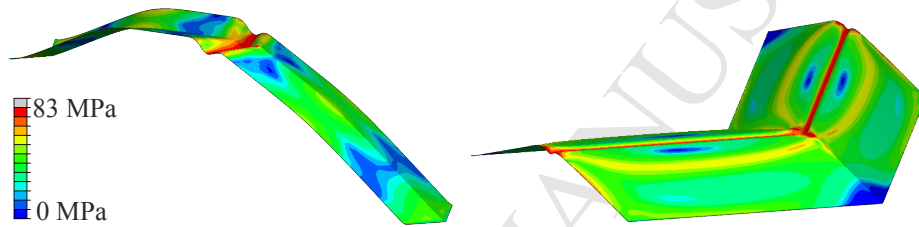


Figure 5: Hinge formation and Von-Mises stress in selected pattern configuration models.



(a) Dimensionless responses, on left; energy absorption suitability, on right



(b) Narrow model E5, on left; wide model E1, on right

Figure 6: Results of side length aspect b^* models.

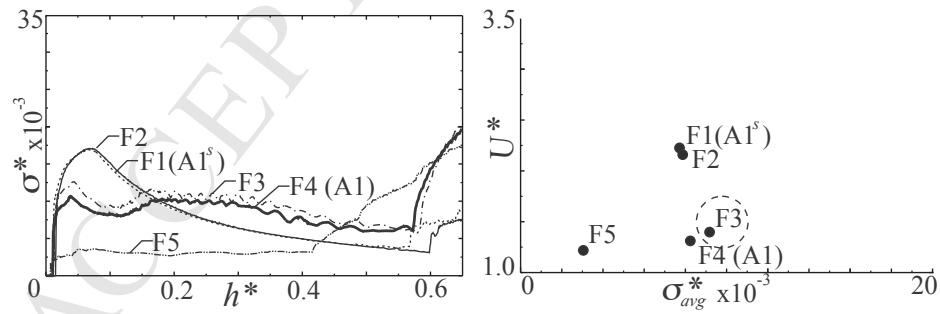


Figure 7: Dimensionless stress-strain responses of indent aspect p^* models, on left; energy absorption suitability, on right.

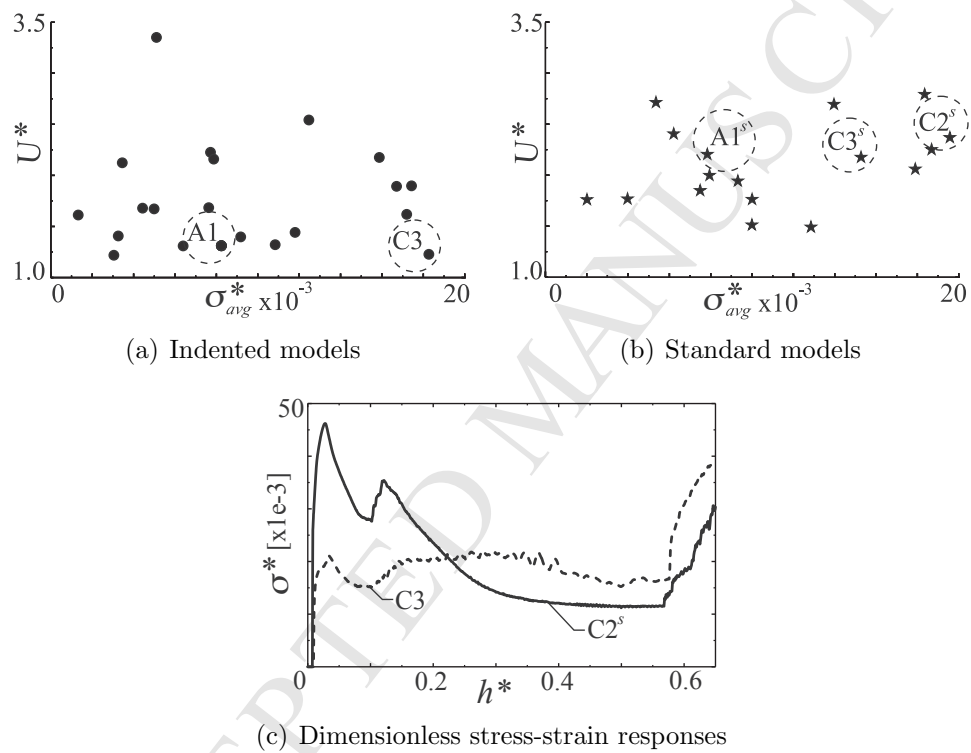


Figure 8: Comparison of optimum indented and standard models.

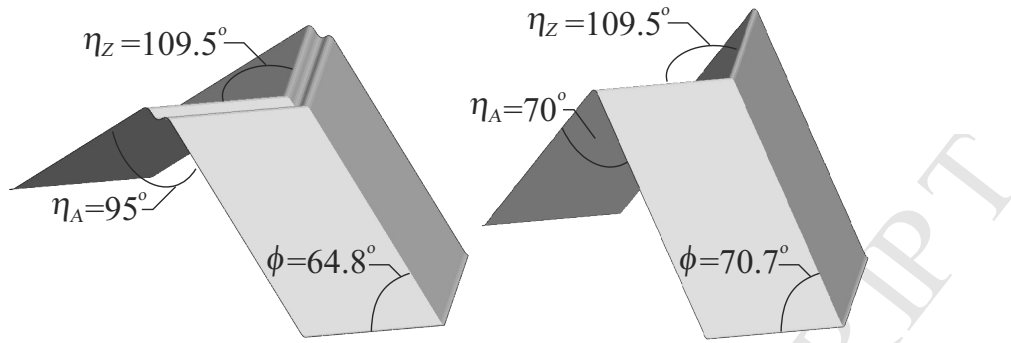
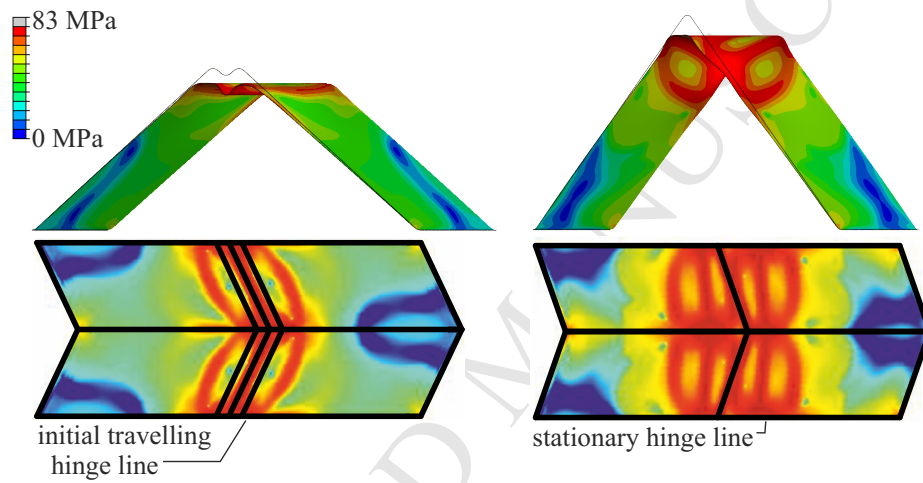
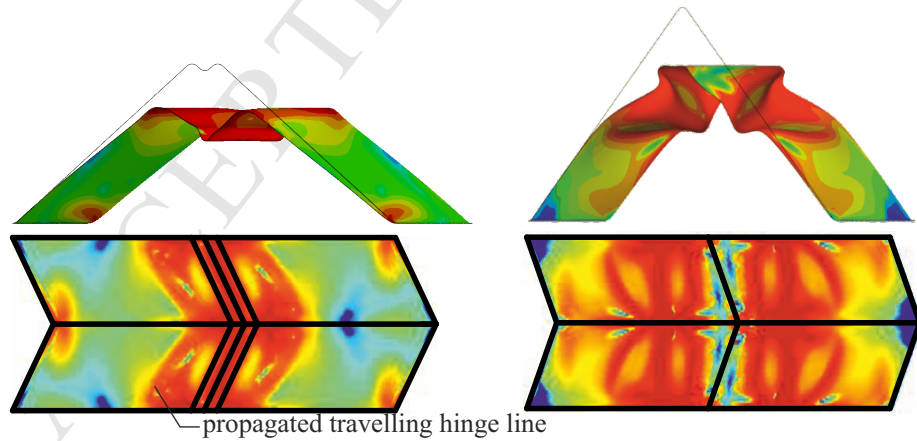
(a) Optimum indented model C3 and standard model C2^s(b) Model C3 and C2^s at $h^* = 10\%$ (c) Model C3 and C2^s at $h^* = 28\%$

Figure 9: Side view and projected view showing Von-Mises stress and hinge propagation on optimal indented (left) and standard (right) foldcores.

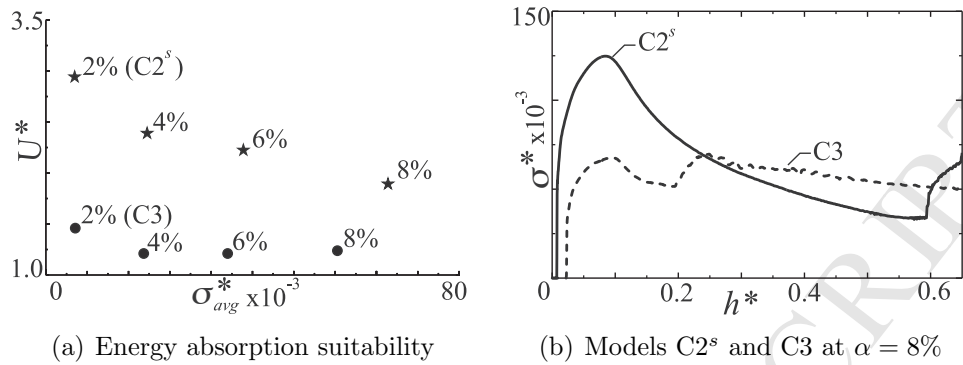


Figure 10: Comparison of optimum foldcore geometries at different densities.

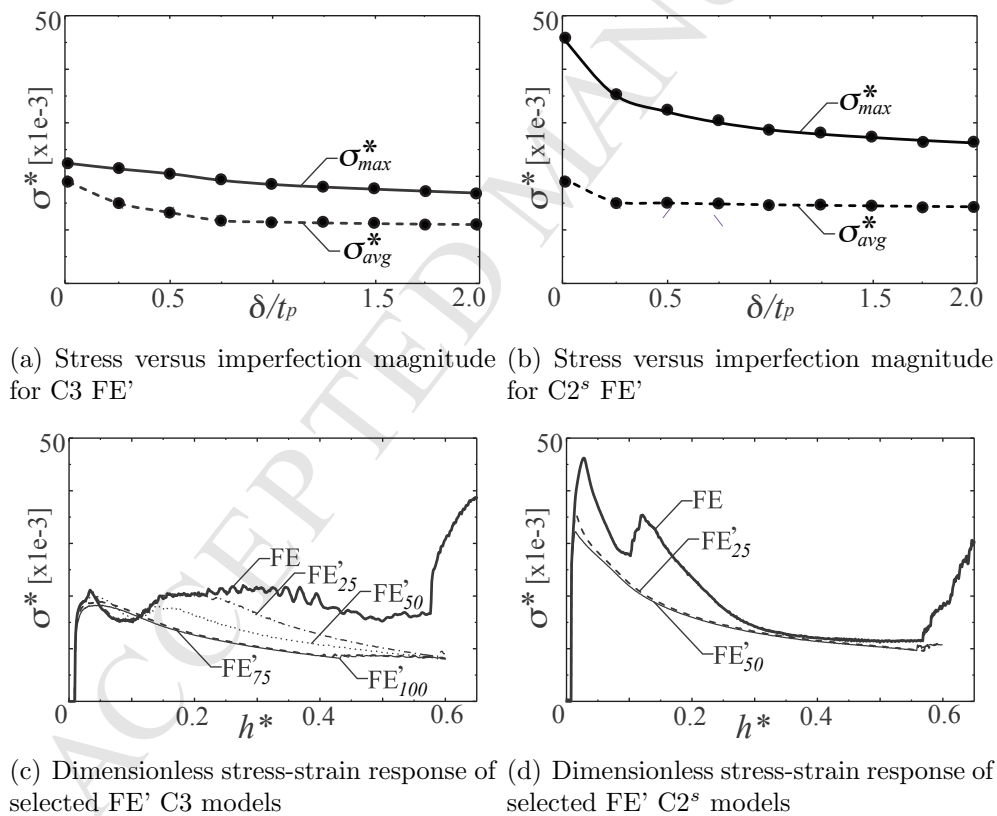
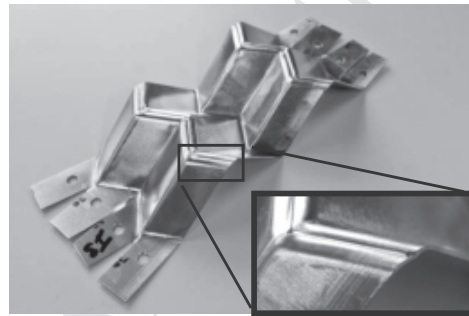


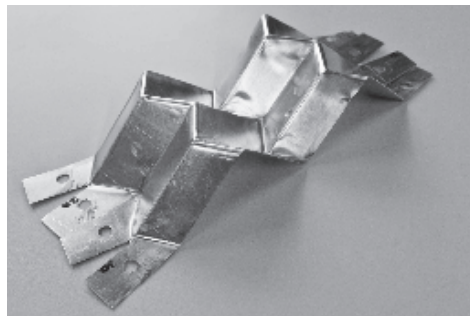
Figure 11: Responses of optimal foldcore geometries with included geometric imperfections.



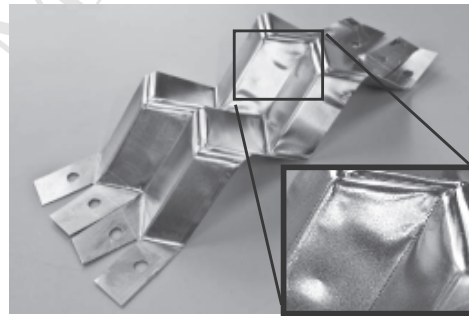
(a) Standard foldcore Mi10



(b) Indented foldcore Ind10



(c) Standard foldcore Mi05



(d) Indented foldcore Ind05

Figure 12: Foldcore prototypes.

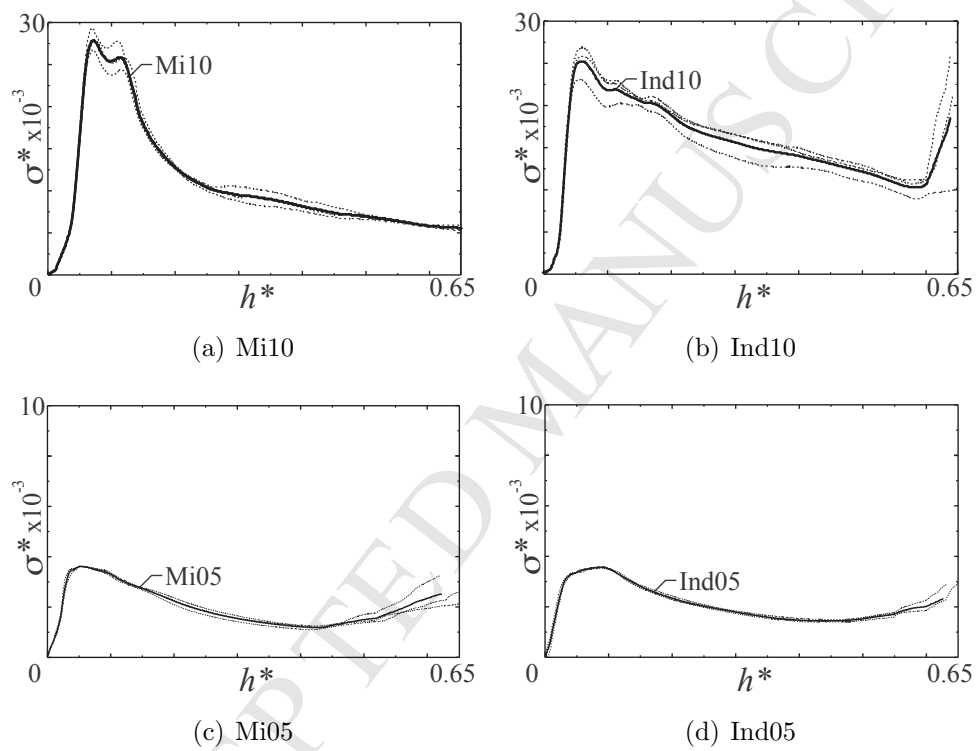
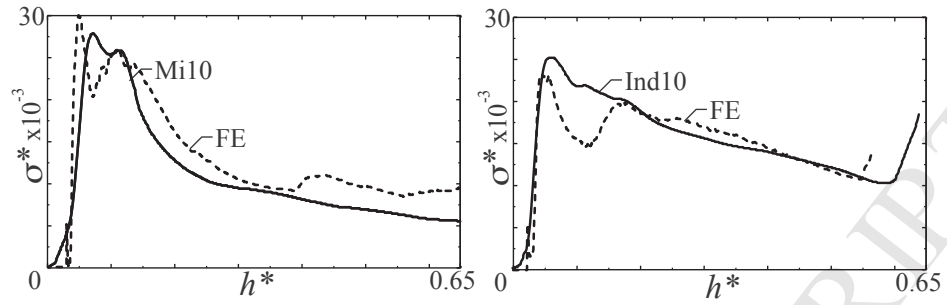
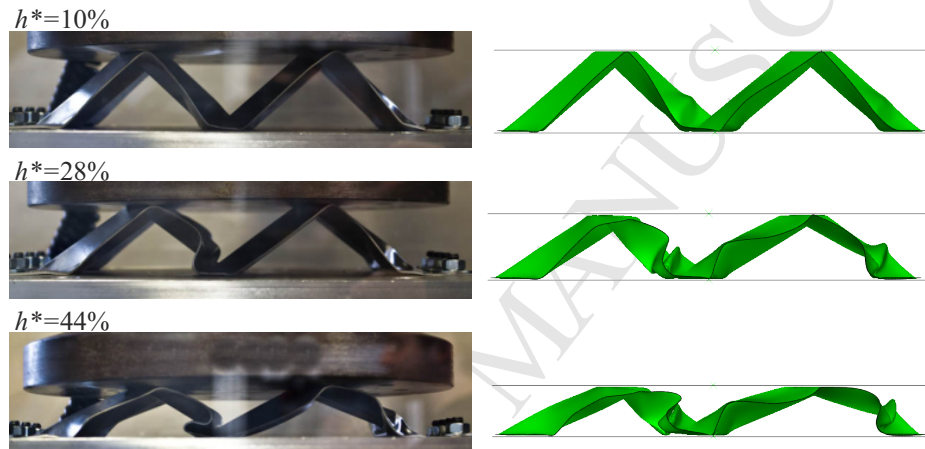


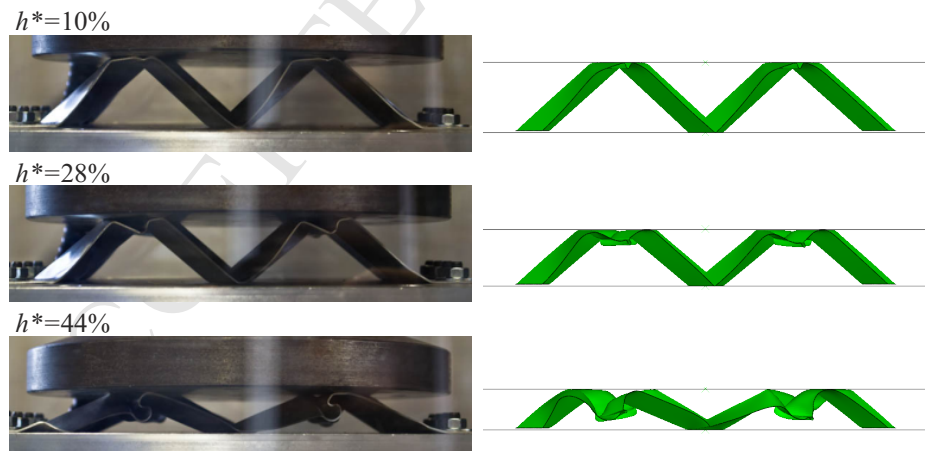
Figure 13: Foldcore prototype dimensionless stress-strain responses.



(a) Dimensionless stress-strain responses of Mi10, on left; Ind10, on right

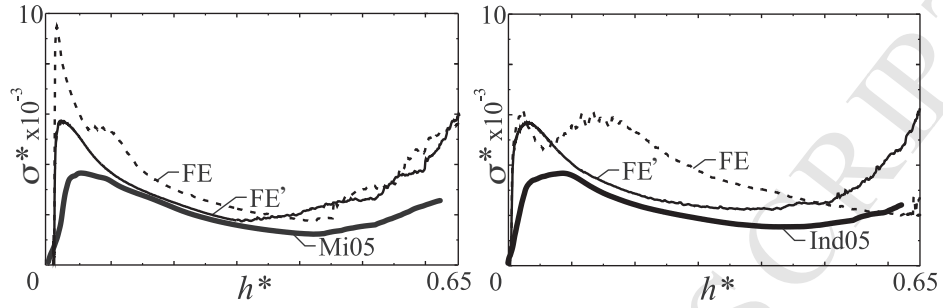


(b) Mi10 experimental and numerical failure modes

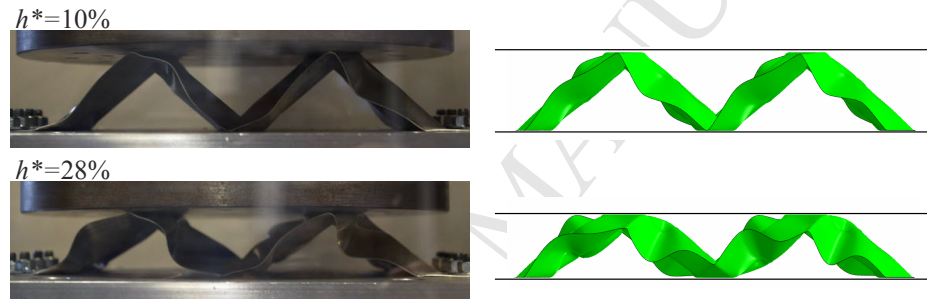


(c) Ind10 experimental and numerical failure modes

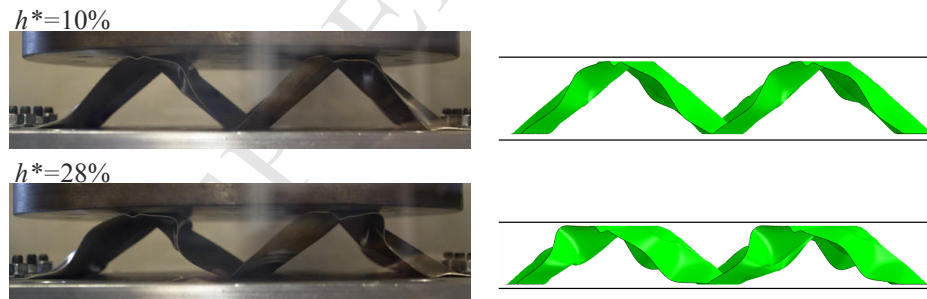
Figure 14: Comparison of numerical and experimental $t_p = 1.0\text{mm}$ foldcore results.



(a) Dimensionless stress-strain responses of Mi05, on left; Ind05, on right

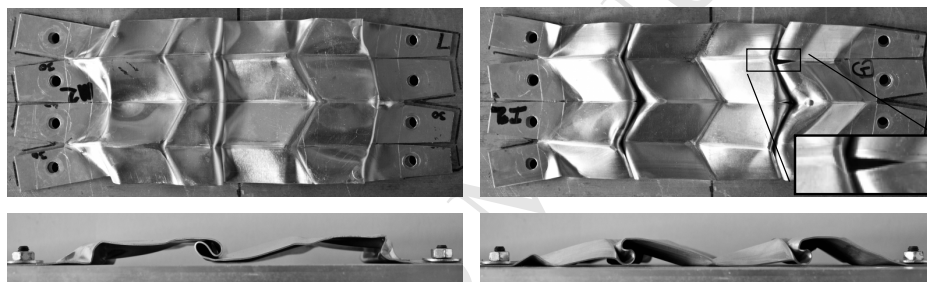
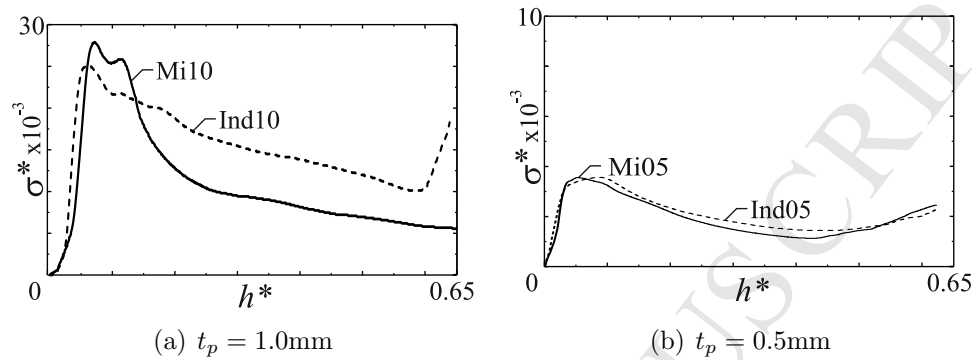


(b) Mi05 experimental and imperfect numerical failure modes

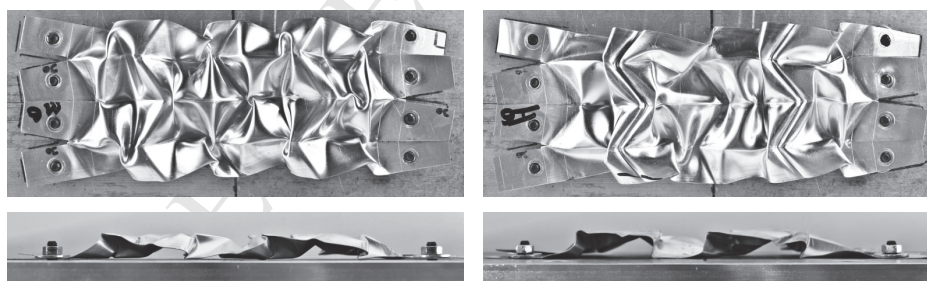


(c) Ind05 experimental and imperfect numerical failure modes

Figure 15: Comparison of FE and FE' numerical and experimental $t_p = 0.5\text{mm}$ foldcore results.



(c) Crushed Mi10 and Ind10 prototypes



(d) Crushed Mi05 and Ind05 prototypes

Figure 16: Comparison of standard and indented prototype responses and failure modes.

Table 1: Parametric study model parameters.

(a) Pattern configuration models				(b) Aspect ratio models			
<i>Model</i>	ϕ ($^{\circ}$)	η_Z ($^{\circ}$)	η_A ($^{\circ}$)	<i>Model</i>	b^*	p^*	α
A1	60.0	109.5	120.0	A1	0.5	0.067	0.04
B1	60.0	42.9	65.0	E1	2.0	0.067	0.04
B2	60.0	69.6	75.0	E2	1.0	0.067	0.04
B3	60.0	90.0	90.0	E4	0.25	0.067	0.04
B5	60.0	117.7	150	E5	0.125	0.067	0.04
C1	77.2	109.2	45.0	F1	0.5	0.0	0.04
C2	70.7	109.6	70.0	F2	0.5	0.017	0.04
C3	64.8	109.4	95.0	F4	0.5	0.05	0.04
C5	56.6	108.3	140	F5	0.5	0.25	0.04
D1	36.9	45.1	120.0				
D2	52.5	90.7	120.0				
D4	70.6	134.9	120.0				
D5	77.1	150.1	120.0				

Table 2: Aluminium true plastic stress-strain data.

(a) Numerical and $t_p = 0.5\text{mm}$ experimental models

Strain	0.0	0.004	0.021	0.054	0.095	0.132
Stress (MPa)	28	43.8	60.0	71.5	78.6	83.3

(b) $t_p = 1.0\text{mm}$ experimental models

Strain	0	0.005	0.014	0.044	0.052
Stress (MPa)	36.8	89.2	98.2	105.5	106.4

Table 3: Results of configuration parameter numerical models.

<i>Model</i>	h_d^*	E_d^* $\times 10^{-3}$	σ_{max}^* $\times 10^{-3}$	σ_{avg}^* $\times 10^{-3}$	U^*
A1	0.57	4.7	10.6	8.2	1.3
B1	0.60	7.5	31.7	12.5	2.5
B2	0.60	10.0	31.5	16.7	1.9
B3	0.58	9.9	27.6	17.2	1.6
B5	0.56	0.7	2.0	1.3	1.6
C1	0.60	9.5	34.5	15.8	2.2
C2	0.60	10.5	32.9	17.4	1.9
C3	0.57	10.4	22.0	18.3	1.2
C5	0.56	1.8	4.4	3.2	1.4
D1	0.51	6.0	16.8	11.8	1.4
D2	0.60	6.5	14.1	10.8	1.3
D4	0.57	2.8	8.2	4.9	1.7
D5	0.58	2.0	7.2	3.4	2.1
E1	0.54	2.4	7.4	4.4	1.7
E2	0.55	3.5	8.2	6.3	1.3
E4	0.60	4.5	12.6	7.6	1.7
E5	0.52	2.6	17.1	5.1	3.4
F1	0.60	4.7	16.9	7.8	2.2
F2	0.60	4.6	17.1	7.6	2.2
F3	0.60	5.5	12.8	9.1	1.4
F5	0.41	1.2	3.6	3.0	1.2

Table 4: Results of equivalent standard models.

<i>Model</i>	h_d^*	E_d^* $\times 10^{-3}$	σ_{max}^* $\times 10^{-3}$	σ_{avg}^* $\times 10^{-3}$	U^*
A1 ^s	0.60	4.7	16.9	7.8	2.2
B1 ^s	0.60	8.4	37.6	14	2.7
B2 ^s	0.60	11.3	42.0	18.8	2.3
B3 ^s	0.60	10.8	36.5	17.9	2.1
B5 ^s	0.60	1.2	3.3	1.9	1.8
C1 ^s	0.60	11.1	51.4	18.5	2.8
C2 ^s	0.60	11.8	46.2	19.7	2.4
C3 ^s	0.60	9.2	32.8	15.3	2.2
C5 ^s	0.60	2.3	6.8	3.9	1.8
D1 ^s	0.53	6.8	19.1	12.9	1.5
D2 ^s	0.60	5.6	17.8	9.3	2.0
D4 ^s	0.60	4.7	15.5	7.9	2.0
D5 ^s	0.60	3.7	14.5	6.2	2.4
E1 ^s	0.60	4.5	13.5	7.4	1.9
E2 ^s	0.55	5.5	14.8	10.0	1.5
E4 ^s	0.60	6.0	17.3	10.0	1.8
E5 ^s	0.53	2.8	14.1	5.3	2.7

Table 5: Optimal foldcore geometries at alternative densities.

t_p (mm)	α	C3			C2 ^s		
		σ_{max}^*	σ_{avg}^* $\times 10^{-3}$	U^* $\times 10^{-3}$	σ_{max}^*	σ_{avg}^* $\times 10^{-3}$	U^* $\times 10^{-3}$
0.13	0.02	7.4	5.1	1.4	14.7	5.0	2.9
0.27	0.04	22.0	18.3	1.2	46.2	19.7	2.4
0.40	0.06	41.8	35.0	1.2	84.5	38.0	2.2
0.53	0.08	69.7	56.4	1.2	124.0	66.0	1.9

Table 6: Optimal foldcore geometries with geometric imperfections.

Model	δ/t_p	C3			C2 ^s		
		σ_{max}^*	σ_{avg}^* $\times 10^{-3}$	U^* $\times 10^{-3}$	σ_{max}^*	σ_{avg}^* $\times 10^{-3}$	U^* $\times 10^{-3}$
FE	0.00	22.0	18.3	1.2	46.2	19.7	2.4
FE'_{25}	0.25	21.1	14.8	1.4	35.5	15.3	2.3
FE'_{50}	0.50	20.3	13.0	1.6	32.2	15.0	2.1
FE'_{75}	0.75	19.0	11.5	1.7	30.1	14.8	2.0
FE'_{100}	1.00	18.3	11.3	1.6	28.7	14.6	2.0
FE'_{125}	1.25	17.8	11.1	1.6	27.9	14.5	1.9
FE'_{150}	1.50	17.4	11.0	1.6	27.3	14.4	1.9
FE'_{175}	1.75	17.0	10.9	1.6	26.7	14.3	1.9
FE'_{200}	2.00	16.7	10.8	1.6	26.2	14.2	1.8

Table 7: Global dimensions of large-scale experimental prototypes.

Model	t_p (mm)	α	Formed (Designed)		
			L (mm)	W (mm)	H (mm)
Mi10	1.0	0.038	182.0 (177.0)	90.0 (87.0)	38.0 (39.0)
Mi05	0.5	0.019	184.0 (177.0)	88.5 (87.0)	37.0 (39.0)
Ind10	1.0	0.040	181.0 (177.0)	90.0 (87.0)	35.0 (36.5)
Ind05	0.5	0.020	180.0 (177.0)	88.5 (87.0)	35.5 (36.5)

Table 8: Results of experimental and numerical models.

	Mi10			Ind10			Mi05			Ind05		
	σ_{max}^* $\times 10^{-3}$	σ_{avg}^* $\times 10^{-3}$	U^*									
Exp	27.9	11.1	2.5	25.2	15.3	1.7	3.7	2.1	1.8	3.7	2.3	1.6
FE	30.2	13.2	2.3	23.3	15.0	1.6	9.4	3.3	2.9	6.2	3.7	1.7
FE'		N/A			N/A		5.7	2.8	2.0	5.7	3.1	1.9